JOURNAL OF SPACECRAFT AND ROCKETS
Vol. 38, No. 6, November–December 2001

Kinetic Analysis of Hypersonic Laminar Separated Flows for Hollow Cylinder Flare Configurations

G. N. Markelov* and M. S. Ivanov†
Institute of Theoretical and Applied Mechanics, 630090, Novosibirsk, Russia

The direct simulation Monte Carlo method was used to study hypersonic laminar flow around hollow cylinder flare configurations. Three configurations with different flare shape and length were considered. This made it possible to estimate the effect of expansion at the trailing end of the flare on the separation region and shock/shock interaction. The results obtained showed that the separation region extent is identical for all configurations for the freestream conditions considered. Nevertheless, the shock/shock interaction region is very close to the end of the flare with the smallest length, which requires particular attention to the computational grid and even to the numerical code. Even small differences in numerical codes may possibly lead to a qualitative change in the flowfield structure. Therefore, for further numerical and experimental studies of this problem, it is necessary to use the configuration with an extended flare because, in this case, the influence of expansion is definitely suppressed. Particular attention was paid to reliability of numerical results and the influence of the grid cell size on calculated flow properties. A cell Knudsen number was used to estimate the quality of the computational grid and to generate a sufficient well-resolved grid.

Nomenclature

C_f	=	skin-friction coefficient
C_H	=	heat transfer coefficient
C_p	=	pressure coefficient
F_{num}	=	number of real molecules represented by a model particle
Kn	=	Knudsen number
Kn_c	=	cell Knudsen number
L	=	reference length, 0.1017 m
M_∞	=	freestream Mach number
N_p	=	total number of model particles
p	=	pressure, Pa
Re	=	Reynolds number
T	=	temperature, K
V	=	velocity, m/s
X_{sep}	=	location of separation point
X, Y	=	Cartesian coordinates, m
Δt	=	time step
ΔX	=	separation region length

Subscripts

w	=	wall
0	=	stagnation quantity
∞	=	freestream quantity

Introduction

ONE of the simple examples of the laminar separated flow induced by shock wave/boundary-layer interaction is the hypersonic flow around a hollow-cylinder flare for low Reynolds number. A flow around such a configuration has been studied in detail in the R5Ch wind tunnel at ONERA.[1,2] In these studies, the Reynolds number was comparatively low ($Re = 1.8916 \times 10^4$) to ensure a laminar flow even near the reattachment point. The pressure and heat flux measurement over the model surface, the oil film visualization, and the electron beam measurements of the density profiles of the flow in different cross sections form a profound basis for validation of numerical methods.

A number of papers have been published that describe the results of modeling this flow using Navier–Stokes equations and the direct simulation Monte Carlo (DSMC) method (see the review[3]). A comparative numerical study of the flow around the hollow-cylinder flare by using both the continuum (Navier–Stokes equations) and kinetic (the DSMC method) approaches was presented in Ref. 4. It was shown that slip conditions for the Navier–Stokes equations should be applied to obtain reasonable agreement with the DSMC results. The use of the boundary conditions for slip velocity and temperature jump has a substantial effect on the entire flowfield for the R5Ch test conditions.[1] A comparison of numerical simulations[2,4,5] with experimental data shows good agreement for the heat flux, though the continuum and kinetic approaches overpredict the pressure values both on the flare and on the hollow-cylinder surface. Concerning the separation region extent prediction, a significant difference between the Navier–Stokes results and experimental data is observed. Therefore, such a situation requires further investigations of laminar flow separation to understand the reasons for this discrepancy. Particularly, new experimental data would be helpful.

Such experiments are planned in the framework of the Research Technology Organization (RTO) Working Group 10 "Technologies for Propelled Hypersonic Flight." This study will be conducted to obtain measurements in the separated laminar flows in the absence of flowfield chemistry for direct comparison with DSMC, Navier–Stokes, and hybrid prediction codes. Two hollow cylinder flare model configurations have been chosen,[6] one of which replicates a configuration used in Ref. 1 and the second of which employs a longer flare to obtain a better defined downstream boundary condition. The low-Reynolds-number test conditions[7] have been selected on the basis of preliminary studies in separated flows to ensure that the flows over these hollow-cylinder flare configurations remain laminar throughout the interaction region.

The main objectives of the present paper are to study an axisymmetric shock wave/laminar boundary-layer interaction for these configurations under laminar flow conditions by the DSMC method and to analyze the influence of the length of the flare and its shape on the separation region extent.

Model Configurations and Test Conditions

Figure 1 shows the model configuration used in experiments,[1] which will be called the base configuration in what follows. To

Presented as Paper 2000-2223 at Fluids 2000, Denver, CO, 19–22 June 2000; received 25 July 2000; revision received 13 April 2001; accepted for publication 20 June 2001.

*Senior Research Scientist, Computational Aerodynamics Laboratory; markelov@itam.nsc.ru.

†Professor, Computational Aerodynamics Laboratory; ivanov@itam.nsc.ru. Associate Fellow AIAA.

Table 1 Test conditions used in simulations

Parameter	Test case 1	Test case 2	Test case 3	R5Ch wind tunnel
M_∞	15.94	11.45	9.13	9.91
p_∞, Pa	3.64	15.52	47.05	6.3
T_∞, K	76.94	123.17	225.67	51.0
Re	8.45×10^3	1.329×10^4	1.36×10^4	1.89×10^4
Kn	2.7×10^{-3}	1.1×10^{-3}	0.8×10^{-3}	0.93×10^{-3}

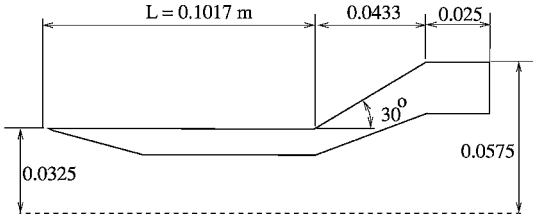

Fig. 1 Model configuration used in Ref. 1 (base model configuration).

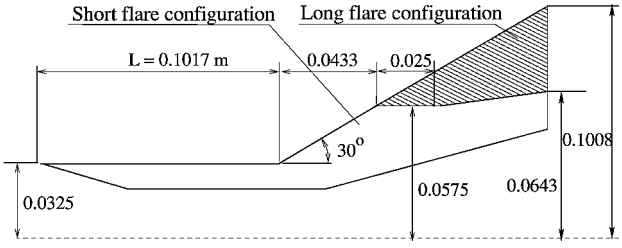

Fig. 2 Model configurations chosen in Ref. 6.

avoid the possible effect of expansion at the end of the conical flare, two other model configurations[6] were used (Fig. 2). The first configuration consists of the base configuration, to which a second, 12-deg flare has been appended. This flare should additionally compress the flow and, thus, decrease the influence of the expansion on shock/shock interaction and the separation region. The other configuration has a significantly increased flare length (see Fig. 2, where the hatched region shows the difference between these models).

The calculations were conducted for these three hollow-cylinder flare configurations under three test conditions[7] listed in Table 1. The test gas is nitrogen, and the Reynolds and Knudsen numbers are based on the length of the hollow cylinder $L = 0.1017$ m. The model surface is assumed to have a constant surface temperature of $T_w = 293$ K for all of the test conditions. Similarity parameters (Mach, Reynolds, and Knudsen numbers) for test case 3 are close to those for R5Ch wind-tunnel conditions, which are also listed in Table 1.

Numerical Approach

The SMILE computational tool[8] was used for modeling the flow over the hollow-cylinder flare. This code is based on the DSMC method[9] and an exact majorant frequency scheme[10] for modeling collision processes. The time between consecutive collisions τ is chosen for each cell from the probability density

$$p(\tau) = \nu_m \exp\{-\nu_m \tau\} \tag{1}$$

Here, the majorant frequency of collisions is

$$\nu_m = [N(N-1)/2][\sigma(g)g]_{\max} \tag{2}$$

where N is the number of molecules in the cell, $\sigma(g)$ is the total collision cross section, and g is the relative velocity of the colliding pair. The variable hard sphere model[9] was used for intermolecular collisions. The Borgnakke–Larsen model[11] with temperature-dependent rotational relaxation number was applied to simulate the energy transfer between the translational and rotational modes (see, for example, Ref. 9). Gas/surface interaction was simulated using the diffuse reflection model with complete accommodation. The freestream flow was modeled as a uniform flow with a Maxwellian

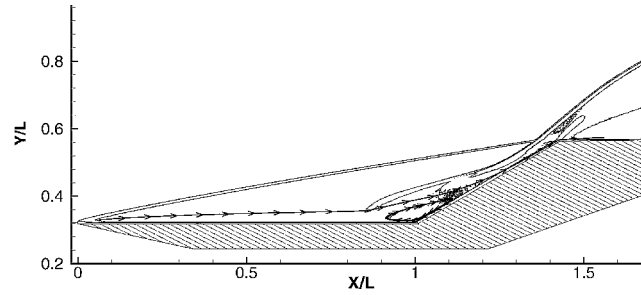

Fig. 3 Pressure gradient contours and selected streamlines (base configurations, test case 3).

distribution function, and vacuum conditions were used at the downstream boundary of the computational domain.

The parallel capability of SMILE allowed the use of a personal computer cluster for computations. The cluster consists of eight personal computers united by Fast Ethernet and powered by the Linux operating system. The Message Passing Interface library was used to organize the information exchange between the processors. The static load balancing[8] with a probabilistic distribution of groups of cells over the processors was employed here. The main advantages of this technique are its low cost and fairly good balancing for a small number of processors. The basic drawback is the violation of data locality: Each processor has cells located at different places of the computational domain, and, in the general case, its neighbors are all other processors; the large number and size of communications between the processors results in a sudden drop of efficiency with increasing the number of processors. Because only eight processors were used in our case, the efficiency was quite high, more than 85%.

Grid Resolution and Subdomain Technique

The general flow structure over the hollow-cylinder flare (base configuration) is depicted in Fig. 3. A separation region arising at the junction of the hollow cylinder and flare is shown by selected streamlines. Pressure gradient contours reveal the expansion region at the end of the conical flare and shock waves. The leading-edge and separation shock waves coalesce into a flare bow shock. Note that the separation shock is highly curved and located very close to the flare surface. It is well known[9] that, in the DSMC method, the linear size of a collision cell should usually not be greater than the local mean free path λ. Violation of this requirement can lead to significant distortion of flow properties. Let us introduce the cell Knudsen number Kn_c; then the collision cell size should satisfy the condition

$$Kn_c = \lambda/\Delta l > 1 \tag{3}$$

where Δl is the linear size of the cell.

The SMILE code employs a procedure of adaptive grid refinement[8] of collision Cartesian cells in the course of calculation to satisfy the preceding condition. However, for a constant total number of model particles, the use of this procedure can lead to formation of very small cells in high-density regions, with only a few model particles in the cell, because the local mean free path is inversely proportional to local density. Though the majorant frequency scheme is a little sensitive to the number of model particles in a cell as compared to the no-time-counterscheme,[9] it still requires the presence of several particles in a cell. Therefore, an additional requirement for the SMILE adaptation procedure is the presence of a certain minimum number of model particles in each collision cell, which ensures correct modeling of collision frequency (usually 5–10 particles per cell for nonreactive flow). As soon as this minumum number of particles in the cell is reached, a further decrease in the linear size of such cells is prohibited. The latter can lead to violation of the aforementioned condition, and in high-density regions, the cell Knudsen number will be smaller than unity, that is, the linear size of such cells will be greater than the local mean free path. The contours of cell Knudsen numbers are plotted in Fig. 4, which shows that we have $Kn_c \sim 0.3$ in the vicinity of the intersection point of the leading-edge shock wave and a separation shock

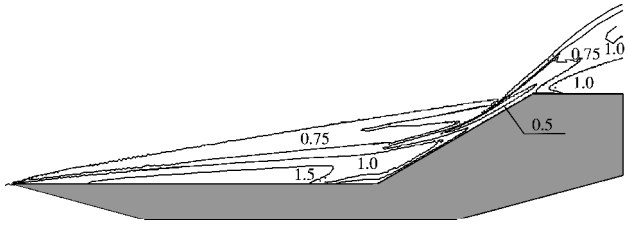

Fig. 4 Cell Knudsen number for coarse grid.

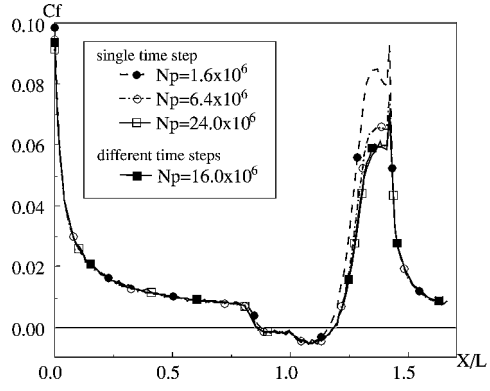

Fig. 5 Skin-friction coefficient (base configuration, test case 3).

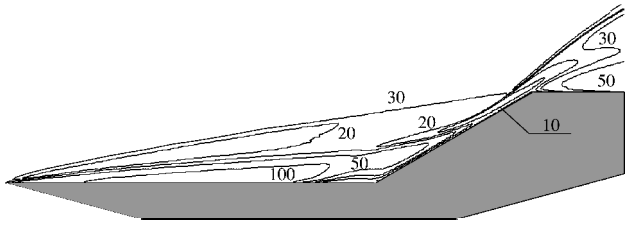

Fig. 6 Number of particles per cell for well-resolved grid with single time step.

wave even if the total number of model particles is $N_p = 1.6 \times 10^6$. Such a coarse grid in high-density regions really leads to distortion of flow properties. For example, the maximum value of the skin-friction coefficient obtained for this total number of model particles was overpredicted by 30% (Fig. 5).

The simplest way to avoid such a situation consists only of significant increasing of the total number of model particles. In our case, an increase in the total number of particles by a factor of four allowed a twofold decrease in the collision cell size in the high-density region along each Cartesian coordinate. This led to some increase in the separation region extent (5%) and a significant decrease (up to 20%) in friction on the flare (Fig. 5). A further increase in the total number of particles (by a factor of four) and the corresponding grid refinement slightly decreased the peak of the skin-friction coefficient but did not affect the separation region extent. In this case, the cell Knudsen number was $Kn_c > 1$ in the entire computational domain. Thus, as long as we have $Kn_c < 1$ in the shock/shock interaction region ($Kn_c \sim 0.3$ for the coarse grid and $Kn_c \sim 0.7$ for the intermediate grid), the skin-friction coefficient is overpredicted.

Sometimes it suffices to have $Kn_c > 1$ only along the direction of flow gradients. In our case, the solution along the hollow cylinder was more sensitive to the linear size of the cell in the normal direction to the surface than to the size along the cylinder surface. For example, the cell size along the surface can be greater than the size normal to the surface by a factor of five. However, the cell shape should be close to square one in the shock/shock interaction region.

On one hand, the use of a great total number of model particles ($N_p = 2.4 \times 10^7$) allowed one, in high-density regions, to obtain cells with $Kn_c > 1$ and containing at least the minimum number of model particles. On the other hand, in low-density regions (near the hollow cylinder), the number of model particles in a cell was much greater than that needed for correct modeling of collision frequency. This is illustrated in Fig. 6. Thus, an increase in the total number of

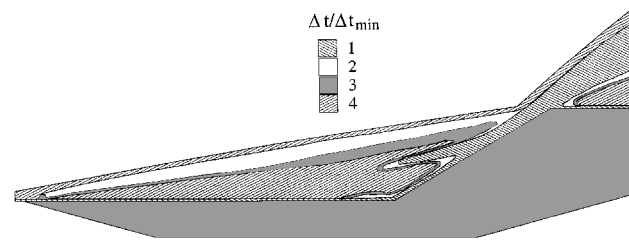

Fig. 7 Subdomains with different time steps.

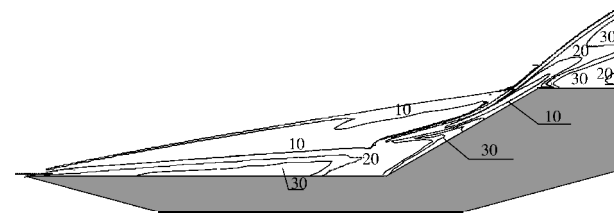

Fig. 8 Number of particles per cell with subdomain technique.

model particles for detailed spatial resolution of flow in high-density regions leads to overpopulation of particles in low-density regions, which significantly decreases the computational efficiency.

To obtain a more uniform distribution of model particles per a cell throughout the computational domain, the latter was divided into subdomains with different time steps. This technique allows one to control the number of particles in each subdomain and is based on the relation $F_{\text{num}}/\Delta t = \text{const}$ satisfied in these subdomains.[12] F_{num} is the number of real molecules represented by a model particle, and an increase in F_{num} with time step Δt leads to a decrease in the total number of model particles in a subdomain. The size and shape of these subdomains are adapted to the flowfield structure during the computational process.[8] Figure 7 shows boundaries of subdomains with different time steps at the steady stage of calculation. In this case, the number of particles per cell is more uniform (cf. Figs. 6 and 8). For hollow-cylinder flare flow this led to a 30% decrease in the total number of model particles and, correspondingly, to a higher computational efficiency. The results obtained with this technique completely coincide with the results for the largest number of model particles with a single time step (see, for example, C_f distribution in Fig. 4). All of the simulation results presented in what follows were obtained using the subdomains with different time steps technique.

Results and Discussion

Rarefaction Effects on Flow Structure

The test conditions in Table 1 allow one to study the flow over a hollow-cylinder flare for various Reynolds and Mach numbers in the near-continuum regime and to demonstrate the effect of flow rarefaction on the formation of a separation region induced by the flare for both model configurations. As is noted in Ref. 6, these configurations are designed so that the separation region is not affected by the trailing end of the flare, and a constant pressure region is formed upstream of the end of the flare. The calculation results for the model configuration with a long flare are plotted in Fig. 9 (normalized pressure contours), which shows that the pressure on the rear half of the flare is really constant. The pressure is only 2–3% higher than the value predicted by inviscid gasdynamics methods. Hence, the pressure mostly depends on the freestream Mach number. Figure 10 shows that the distribution of the pressure coefficient C_p along the hollow cylinder ($X/L < 0.9$) and on the major part of the flare ($X/L > 1.6$) is almost identical for all three test conditions. The pressure peak increases with both freestream Mach number and Reynolds number. For considered test cases, the highest pressure coefficient corresponds to $M_\infty = 16$. Next is $M_\infty = 11$, and the least value of C_p corresponds to $M_\infty = 9$. The cases differ in the Mach number (by a factor of 1.75) and Reynolds number (by a factor of 1.6). Therefore, to show the pure influence of the Reynolds number, additional calculations were performed for $M_\infty = 15.94$. Figure 11 shows that an increase in the Reynolds number leads not only to a pressure increase, but that the peak becomes sharper and moves upstream.

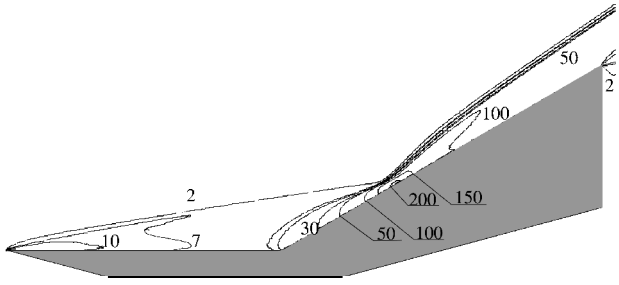

Test case 1

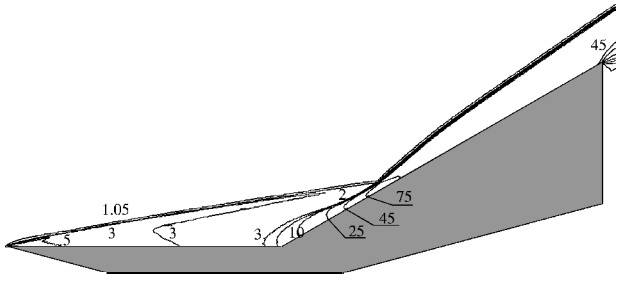

Test case 2

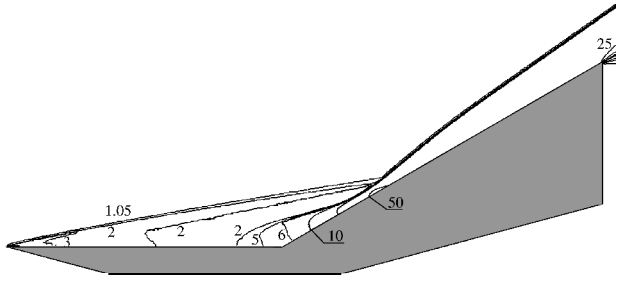

Test case 3

Fig. 9 Normalized pressure contours (configuration with long flare).

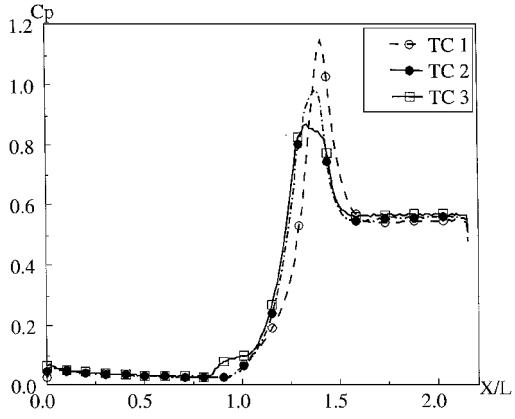

Fig. 10 Pressure coefficient (configuration with long flare).

A constant pressure region over the second conical flare is also formed in the flow over the model configuration with a short flare (see, for example, Fig. 12). However, the value of the pressure coefficient along this part of the flare (Fig. 13) is significantly lower than that for the model configuration with a long flare.

The presence of a plateau in the distribution of C_p for test case 3 (see Fig. 10 or Fig. 13) is typical of a developed separated flow. Figure 14 shows the distribution of the skin-friction coefficient for both configurations. A vast separation region is formed only in test case 3. For test case 2, negative values of the friction coefficient are observed in a small vicinity of the cylinder/flare junction. A further decrease in the Reynolds number (case 1) leads to a completely attached flow. Thus, only test case 3 is of interest for subsequent study of the effect of the flare shape and length on shock/shock interaction and separation region extent. Though the Reynolds numbers for cases 2 and 3 are almost identical, a developed separation region is observed only for the lowest Knudsen number, $Kn = 0.8 \times 10^{-3}$.

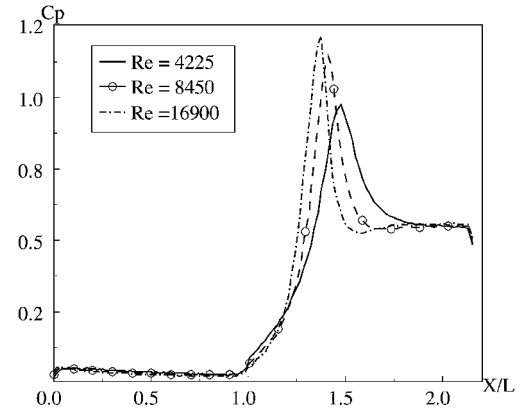

Fig. 11 Influence of Reynolds number on pressure coefficient (M_∞ = 15.94).

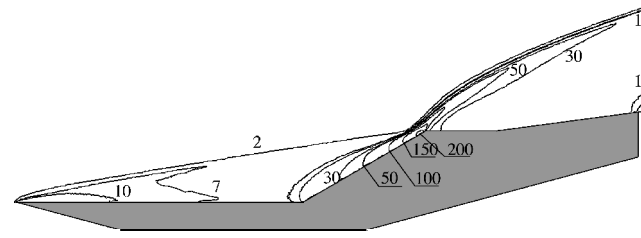

Fig. 12 Normalized pressure contours (configuration with short flare, test case 1).

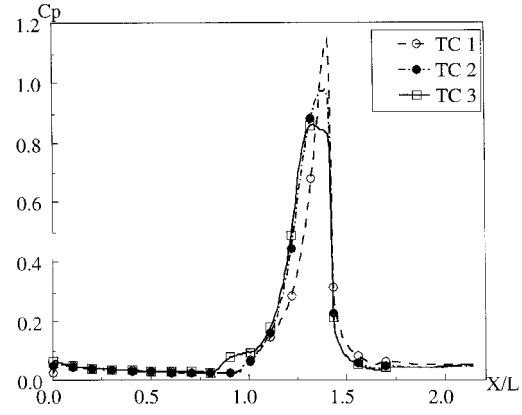

Fig. 13 Pressure coefficient (configuration with short flare).

Flow Around the Base Model Configuration

One of the main objectives of the experimental study[6] is the obtaining of measurements for test conditions close to the R5Ch wind-tunnel conditions.[1] In Ref. 1, the value of the Mach and Knudsen numbers are close to those in test case 3. Thus, it is interesting to compare directly the flow around the base model configuration for test case 3 and R5Ch test conditions and then study the effect of the flare shape and length for test case 3.

Figure 15 shows the pressure flowfields for these two test conditions. At first glance, the flow structure is identical, and there is only a small difference in the position of the intersection point I of the leading-edge shock wave and the separation shock wave. For test case 3, this point is located at a radial position $Y/L = 0.565$ corresponding to the flare radius, whereas for R5Ch flow conditions this point is located higher ($Y/L = 0.59$) and farther downstream. This difference in the position of the intersection points can be attributed to the different slope of the leading-edge shock wave for these conditions. The freestream Mach and Knudsen numbers are rather close, but the temperature factor T_w/T_0 differs by more than thrice for R5Ch conditions and case 3 ($T_w/T_0 = 0.279$ and $T_w/T_0 = 0.073$, respectively). Therefore, the boundary-layer thickness for test case 3 is smaller, which, in turn, leads to a decrease in the leading-edge shock wave slope. A zoom view of the flow

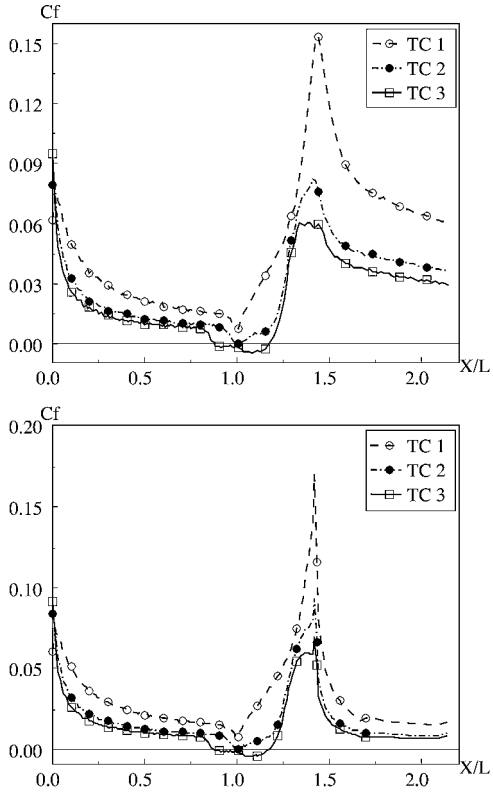

Fig. 14 Skin-friction coefficient (top, long flare, and bottom, short flare).

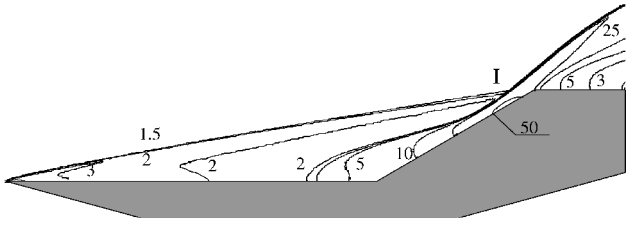

Test case 3

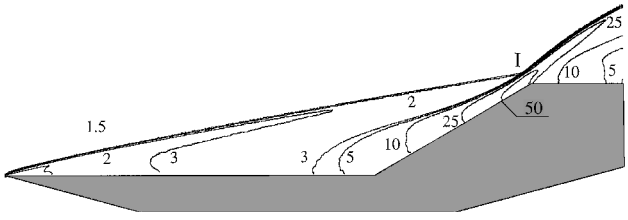

R5Ch wind tunnel conditions

Fig. 15 Normalized pressure contours (base model configuration).

region near the flare in Fig. 16 reveals a qualitative difference in the flow structure. For test case 3, the pressure gradient flowfield shows shock waves, expansion at the end of the conical flare, and a narrow region P, emanating from the intersection point. It is well known[13] that an intersection of shocks of the same family produces not only a joint shock but also Prandtl–Meyer expansion or a weak shock to match the pressure increase through two shocks and through the joint shock. In our case, the region P corresponds to Prandtl–Meyer expansion (Fig. 16). For R5Ch flow conditions, it is impossible to identify such a region, though it has to exist judging by an analysis of shock angles. The plausible reason is the influence of expansion at the end of the conical flare on the flow near the intersection point. Figure 16 shows that the expansion has no direct effect on the flow. Possibly, the expansion produces an indirect effect by decreasing the boundary-layer thickness, and this effect will vanish if the flare length is somewhat increased. To verify this, a calculation was performed for the flow over a configuration whose

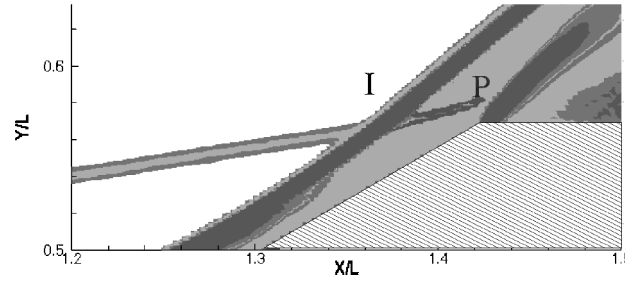

Test case 3

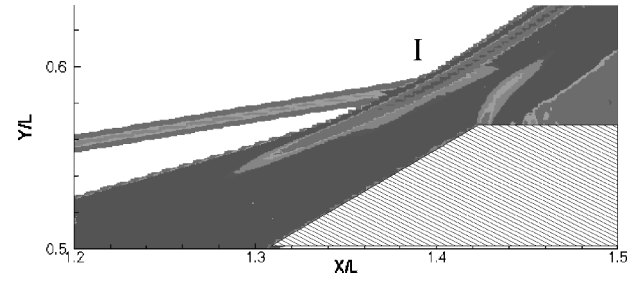

R5Ch wind tunnel conditions

Fig. 16 Zoom of region near end of flare (pressure gradient flowfield).

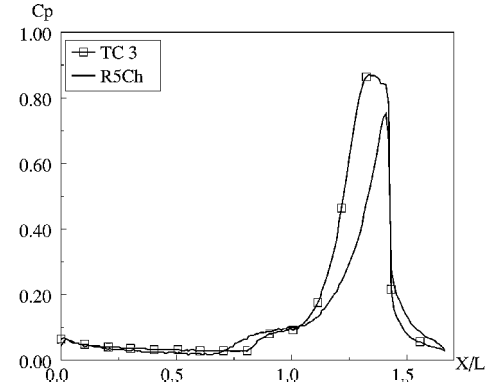

Fig. 17 Pressure coefficient (base model configuration).

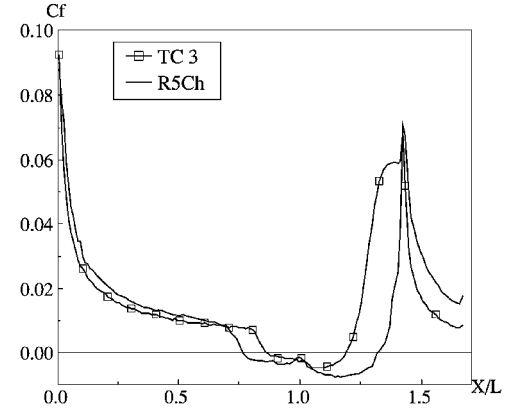

Fig. 18 Skin-friction coefficient (base model configuration).

flare length was extended by a factor of 1.7. The calculation results showed that an increase in the flare length really led to an increase in the separation-region extent (by 17%) and an emergence of well-resolved Prandtl–Meyer expansion emanating from the intersection point.

The pressure peak (Fig. 17) for test case 3 is higher and is located on the flare, whereas the position of the peak of the pressure coefficient for R5Ch conditions coincides with the end of the conical flare. The distribution of the friction coefficient plotted in Fig. 18 demonstrates a significant difference in the separation point position ($X_{sep}/L = 0.72$ and 0.86 for R5Ch and case 3 conditions,

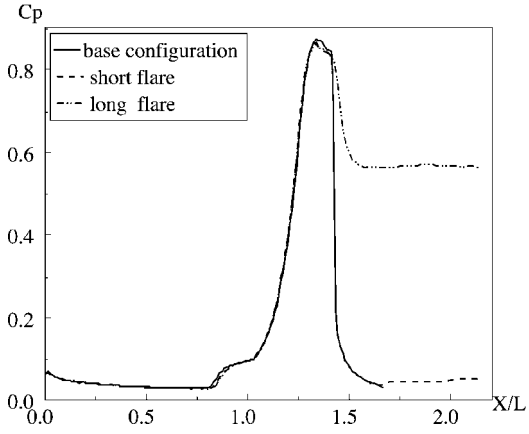

Pressure coefficient

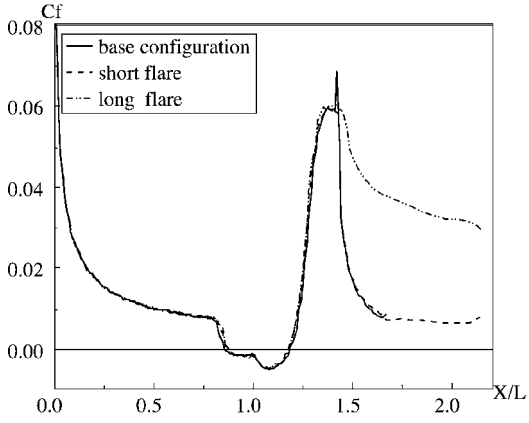

Skin-friction coefficient

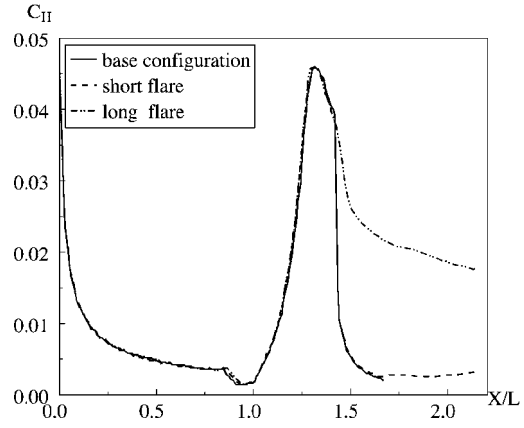

Heat transfer coefficient

Fig. 19 Influence of shape on aerothermodynamics characteristics.

respectively) and the separation-region extent ($\Delta X/L = 0.55$ and 0.33) for these two flow conditions. Note that the distribution of C_f for test case 3 has a small plateau before the peak corresponding the end of the conical flare. Summarizing the differences observed in flow properties for these cases, we can assume that for test case 3 an increase in the length of the flare or a change in its shape should not affect the shock/shock interaction and separation region extent.

Influence of Shape and Length of the Flare

The preceding assumption will be confirmed in this section by direct comparison of the results for the base model configuration and two other model configurations for test case 3. Different dimensions of the flare for these configurations caused a significant increase in the computational domain and, as a consequence, an increase in the computational cost. The calculation time for the flow around the model configuration with a short flare is twice as long as for the base model configuration, and the calculation time for

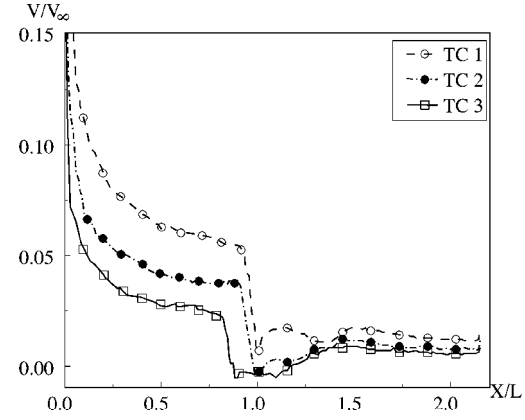

Fig. 20 Gas velocity at wall (configuration with long flare).

the model configuration with a long flare is twice as long as for the configuration with a short one.

The distributed aerothermodynamic characteristics in Fig. 19 confirmed the assumption. For all three model configurations, the distributed characteristics coincide up to $X/L = 1.426$, which is the coordinate of the end of the conical flare for the base model configuration. For the base model configuration and the configuration with a short flare, this coincidence is observed farther up to the end of the cylindrical part of the flare ($X/L = 1.672$). This coincidence of results for the three model configurations is a consequence of the fact that, for test case 3, the intersection point of the leading edge and separation shock waves is not affected by expansion at the end of the conical flare even for the base model configuration.

As was noted, the position of this point depends significantly on the position of the leading-edge shock wave, which is substantially affected by rarefaction.[4] The gas velocity at the wall plotted in Fig. 20 shows that, though the slip velocity decreases with decreasing Knudsen number, it still remains quite significant for test case 3 ($Kn = 0.8 \times 10^{-3}$, $Re = 1.36 \times 10^4$, and $M_\infty = 9.13$). Therefore, the use of the Navier–Stokes equations for description of the flow over a hollow-cylinder flare with no-slip boundary conditions can lead to a qualitative change in the position of the intersection point and, as a consequence, to a possible effect of the shape of the flare on the separation region extent.

Conclusions

Within the framework of the RTO, there are plans to study experimentally separated laminar flows for subsequent validation of numerical codes. In this work, the DSMC method was used to study hypersonic laminar flow around hollow-cylinder flare configurations under flow conditions considered by RTO. It is well known that the calculated properties of the flow over such configurations are very grid sensitive. Therefore, particular attention was paid to reliability of numerical results and the influence of the grid cell size on calculated flow properties. It was shown that the minimum value of the cell Knudsen number has to be greater than unity within the entire computational domain to obtain a grid-independent solution. The simplest way to reach this is to increase the total number of model particles. However, this way leads to unnecessary computational costs because the number of model particles in a cell in low-density regions (near the hollow cylinder) is much greater than that needed for correct modeling of the collision frequency. The use of subdomains with different time steps allowed us to obtain a more uniform distribution of model particles per cell throughout the computational domain and, as a consequence, to reduce the total number of particles by 30%.

The present numerical studies show that an attached flow over the configurations is observed for flow conditions with the highest Knudsen number of this study. For the test case with an intermediate Knudsen number, a separation region just begins to form. As is shown in Ref. 4, the Navier–Stokes equations, even taking into account slip boundary conditions, overpredict the separation region extent. Probably, this test case is also important from the viewpoint

of numerical analysis because it offers the possibility of a detailed study of quantitative and qualitative influence of the initial effects of rarefaction (i.e., slip velocity and temperature jump for Navier–Stokes equations) on the formation of the separation region.

The test case with the lowest Knudsen number for which a developed separation region is observed is obviously of great interest for the validation of DSMC, Navier–Stokes, and hybrid codes. The simulation revealed that in this case the flow in the intersection point of leading-edge shock and separation shock is not influenced by the expansion at the end of the conical flare. As a result, the length of the separation region is independent of the length of the flare and its shape. For example, the distributed aerothermodynamic characteristics (C_p, C_f, and C_H) coincide for all three model configurations up to $X/L = 1.42$, corresponding to the end of the shortest conical flare.

From the computational point of view, the base model configuration used in the experimental study[1] is preferable for verification of different numerical codes due to the lowest computational cost. However, the position of the intersection point of the shocks is very close to the end of the conical flare, and even small differences in numerical codes can lead to a qualitative change in the flowfield structure. For example, the use of the Navier–Stokes equations results in the prediction of a greater slope of the leading-edge shock wave, and the separation region can be affected by expansion. Therefore, it is necessary to use the model configuration with an extended flare because, in this case, the influence of expansion is definitely suppressed.

Acknowledgments

This work was supported by INTAS Grant 99-00749 and Russian Foundation for Basic Research Grant 00-01-00824. This support is gratefully acknowledged.

References

[1]Chanetz, B., "Study of Axisymmetric Shock Wave/ Boundary Layer Interaction in Hypersonic Laminar Flow," ONERA, TR RT 42/4362 AN, 1995.

[2]Chanetz, B., Bur, R., Pot, T., Pigache, D., Gorchakova, N., Moss, J., and Schulte, D., "Study of the Shock Wave/Boundary Layer Interaction in Low Density Hypersonic Flow: Comparison Between Flowfield Measurements and Numerical Results," *Proceedings of the 21st International Symposium on Rarefied Gas Dynamics*, edited by R. Brun, R. Campargue, R. Gatignol, and J.-C. Lengrand, Vol. 2, CEPADUES-Editions, Toulouse, France, 1999, pp. 537–544.

[3]Grasso, F., and Marini, M., "Synthesis of T2-97 Hollow-Cylinder Flare Problem," *Proceedings of the First Europe–U.S. High-Speed Flowfield Database Workshop (Part 2)*, edited by S. Borrelli, M. Marini, F. Grasso, and J. Periaux, AIAA, Reston, VA, 1998, pp. 213–221.

[4]Markelov, G. N., Kudryavtsev, A. N., and Ivanov, M. S., "Continuum and Kinetic Simulation of Laminar Separated Flow at Hypersonic Speeds," *Journal of Spacecraft and Rockets*, Vol. 37, No. 4, 2000, pp. 499–506.

[5]Moss, J., Olejniczak, J., Chanetz, B., and Pot, T., "Hypersonic Separated Flows at Low Reynolds Number Conditions," *Proceedings of the 21st International Symposium on Rarefied Gas Dynamics*, edited by R. Brun, R. Campargue, R. Gatignol, and J.-C. Lengrand, Vol. 2, CEPADUES-Editions, Toulouse, France, 1999, pp. 617–624.

[6]Holden, M., "Experimental Studies of Laminar Separated Flows Induced by Shock Wave/ Boundary Layer and Shock/Shock Interaction in Hypersonic Flows for Computational Fluid Dynamic Validation," AIAA Paper 2000-0930, Jan. 2000.

[7]Knight, D., "CFD Validation for Hypersonic Flight," Stage 1 Rept., 2000, URL: http://coewww.rutgers.edu/∼wg 10.

[8]Ivanov, M. S., Markelov, G. N., and Gimelshein, S. F., "Statistical Simulation of Reactive Rarefied Flows: Numerical Approach and Applications," AIAA Paper 98-2669, June 1998.

[9]Bird, G. A., *Molecular Gas Dynamics and the Direct Simulation of Gas Flows*, Clarendon, Oxford, 1994.

[10]Ivanov, M. S., and Rogasinsky, S. V., "Theoretical Analysis of Traditional and Modern Schemes of the DSMC Method," *Proceedings of the 17th International Symposium on Rarefied Gas Dynamics*, edited by A. E. Beylich, VCH, Aachen, Germany, 1991, pp. 629–642.

[11]Borgnakke, C., and Larsen, P. S., "Statistical Collision Model for Monte Carlo Simulation of Polyatomic Gas Mixture," *Journal of Computational Physics*, Vol. 18, No. 3, 1975, pp. 405–420.

[12]Olynic, D. P., Hassan, H. A., and Moss, J. N., "Grid Generation and Adaptation for the Direct Simulation Monte Carlo Method," AIAA Paper 88-2734, June 1988.

[13]Shapiro, A. H., *The Dynamics and Thermodynamics of Compressible Flow*, Ronald, New York, 1953, p. 558.

J. C. Taylor
Associate Editor